ADVANCED MATERIALS INTERFACES
Open Access
www.advmatinterfaces.de

Transient Formation of Single Layer Diamond During Friction Force Microscopy of SiC-Supported Epitaxial Graphene

*Mohammad Zarshenas, Takuya Kuwahara, Bartosz Szczefanowicz, Andreas Klemenz, Leonhard Mayrhofer, Lars Pastewka, Gianpietro Moras, Roland Bennewitz, and Michael Moseler**

Carbon allotropes are crucial to advanced interfaces to control friction and wear because of their unique range of mechanical properties: from diamond's hardness to graphite's lubricity. Friction force microscopy (FFM) is reported for diamond tips sliding on SiC(0001)-supported epitaxial graphene. A sharp friction increase is observed at a threshold normal force, linked to an intermittent graphene rehybridization. Comparing the FFM response of a diamond tip to that of a previously studied silicon tip with a comparable radius reveals a similar abrupt friction increase, though at roughly half the threshold force. Atomistic simulations of SiC(0001)-supported graphene sliding against hydroxylated amorphous carbon (a-C) and silicon oxide show low shear stress at low pressures for both systems. The shear stress increases at higher pressures due to bond formation between graphene and the counterbody. For a-C, the transition threshold shifts to higher pressures, consistent with FFM results. In simulations with high normal pressures, epitaxial graphene undergoes a structural transformation into single-layer diamond, contributing to the abrupt increase in friction. The graphene structure recovers after lifting the a-C counterbody, demonstrating structural robustness under tribological stress. These findings provide insights into the stability of low-friction interfaces between epitaxial graphene and key materials for current micro-electro-mechanical systems (MEMS)

1. Introduction

Flat graphene layers are known to exhibit very low friction under various conditions. Incommensurate contact reduces lateral friction, leading to structural superlubricity.[1–3] Weak interfacial bonding reduces friction when no strong chemical interactions occur at the interface.[4,5] Vacuum or dry environments enhance superlubricity by minimizing contamination and adsorbed layers.[6,7] At the nanoscale or microscale, atomic force microscopy (AFM) and friction force microscopy (FFM) measurements confirm ultra-low friction due to weak interlayer van der Waals forces.[8,9] Controlled normal load plays a key role, as graphene retains superlubricity at low loads but may lose it under high pressures.[1,9] Finally, temperature influences graphene's frictional response, with variations in this parameter affecting its superlubric behavior.[8] The strong covalent in-plane C—C bonds

M. Zarshenas, A. Klemenz, L. Mayrhofer, G. Moras, M. Moseler
Fraunhofer IWM
MikroTribologie Centrum µTC
Wöhlerstraße 11, 79108 Freiburg, Germany
E-mail: michael.moseler@iwm.fraunhofer.de

M. Zarshenas, M. Moseler
Institute of Physics
University of Freiburg
Hermann-Herder-Straße 3, 79104 Freiburg, Germany

The ORCID identification number(s) for the author(s) of this article can be found under https://doi.org/10.1002/admi.202500511

DOI: 10.1002/admi.202500511

T. Kuwahara
Department of Mechanical Engineering
Osaka Metropolitan University
1-1 Gakuen-cho, Sakai, Naka-ku 599–8531, Japan

B. Szczefanowicz
Marian Smoluchowski Institute of Physics
Jagiellonian University
Krakow 30–348, Poland

B. Szczefanowicz, R. Bennewitz
INM – Leibniz Institute for New Materials
Campus D2 2, 66123 Saarbrücken, Germany

B. Szczefanowicz, R. Bennewitz
Saarland University
Physics Department
Campus D2 2, 66123 Saarbrücken, Germany

L. Pastewka
Department of Microsystems Engineering
University of Freiburg
Georges-Köhler-Allee 103, 79110 Freiburg, Germany

provide graphene with high stability against chemical and mechanical wear. Therefore, graphene is an intriguing 2D model system to investigate mechanisms which can lead to ultra-low friction.[10–13] Epitaxial graphene on SiC(0001) exhibits super-low friction due to its weak out-of-plane interactions.[14] Using FFM, Szczefanowicz et al. studied the tribological behavior of epitaxial graphene using silicon tips with a SiO_2 surface layer, revealing a sudden transition between a low- and high-friction regime.[15] They found, with accompanying self-consistent charge density functional tight-binding (DFTB) simulations,[16] that the threshold pressure for entering the high-friction regime was 10 GPa and that the atomic configuration of the amorphous SiO_2 played a crucial role in determining covalent bond formation in the transition regime. The study also highlighted the importance of understanding chemical aspects of the tribological behavior of graphene across various sliding regimes.

While this previous research focused on the sliding behavior between a silicon tip and epitaxial graphene,[15] the present study aims to investigate the sliding interaction between epitaxial graphene on SiC(0001) and a diamond tip covered by an a-C surface layer. The use of a diamond tip provides an alternative material system for exploring the mechanisms leading to ultra-low friction, as the bonding mechanisms and material properties of the a-C differ from those of the SiO_2 surface layer. By comparing the behavior of a diamond and a silicon tip, we aim to elucidate the influence of different bonding mechanisms and material properties on sliding behavior and shear stresses. Overall, this investigation contributes to a deeper understanding of the mechanisms governing the sliding interaction between a-C covered diamond and epitaxial graphene, shedding light on the factors influencing friction and providing valuable insights for the design of low-friction interfaces – for instance in modern MEMS applications.

2. Results

2.1. Experiments

Low friction with a linear increase as a function of applied normal force and with fluctuations in the magnitude of the frictional force was observed for a diamond tip for normal forces up to 400 nN (red diamonds in **Figure 1**). Beyond 400 nN, there is a sudden increase in the friction force, reaching up to 2.5 nN. In a second experiment with the same tip, the sudden increase to higher friction forces was observed at a normal force of 500 nN (blue triangles in Figure 1). Experiments with other diamond tips showed the transition at 230 nN (Adama tip) and 310 nN (Nanosensors DT-FMR tip).

The experiments were performed on atomically smooth terraces of single-layer graphene with no signatures of defects, which were selected by low-load overview scans (see description in ref. [15] and example in Figure S1c of the Supporting Information (SI)). Please note that the graphene did not rupture during the experiments with the diamond tip. The integrity of the graphene layer was confirmed by the observation of periodic atomic-scale stick-slip patterns in the measured lateral force (Figure S2 of the SI). Experiments with diamond tips performed at loads higher than those reported in Figure 1 show that rupture

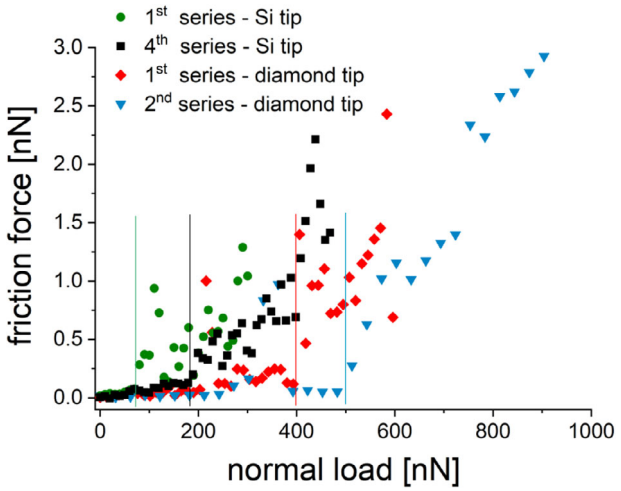

Figure 1. Friction force as a function of the applied normal force recorded with a silicon and a diamond tip sliding over epitaxial graphene on a SiC(0001) substrate. Results are shown for the first series with fresh tips and later series with the same tips. Vertical lines indicate the transition forces discussed in the text. Please note that the data for silicon tips are shown for comparison. They have been published and discussed.[15]

of the graphene leads to large irregular fluctuations in the lateral force signal (Figure S1 of the SI).

We compare our FFM experiments using a diamond tip with previously published results from an identical study using a silicon tip.[15] Figure 1 also displays the friction force acting on a Si tip (initially and after repeated FFM scans – see green disks and black squares) as a function of normal pressure, and compares it with the diamond tip FFM experiment (red squares). For the Si tip, Szczefanowicz and coworkers[15] observed an initial linear low-friction regime up to a force of 80 nN, followed by an abrupt increase in the average slope of the friction versus normal pressure curve. High-friction values generally increase with pressure but exhibit significant scatter, occasionally returning to the low-friction regime. After repeating the friction force experiment three more times, the transition to high friction occurs at a higher normal force of 180 nN (4th series in Figure 1). This effect was explained by blunting of the Si tip. Please note that all three values for the transition force of diamond tips reported here (230 – 400 nN) are larger than the four values for silicon tips (60 – 180 nN) of ref. [15]. To compare experimental results with material properties and simulations, conversion of transition forces F_N into a normal pressure would be useful. Unfortunately, the validity of continuum mechanics models for contacts at the nanometer scale is limited, both because of the unknown atomic configuration of the tip apex[17] and because of the layered nature of the graphene/SiC[0001] interface.[18] Neglecting these limitations, the maximum pressure p_0 in a Hertzian contact is given by

$$p_0 = \frac{1}{\pi}\left(\frac{6F_N E^{*2}}{R^2}\right)^1 \text{ with } \frac{1}{E^*} = \frac{1-\nu^2_{\text{grSiC}}}{E_{\text{grSiC}}} + \frac{1-\nu^2_{\text{a-C}}}{E_{\text{a-C}}} \quad (1)$$

For an estimate, we assume the values of 6H-SiC ($E_{gr/SiC}$ = 400 GPa, $\nu_{gr/SiC}$ = 0.16) and of a low-density a-C[19] with ρ = 2.1–2.2 g cm^{-3} (E_{a-C} = 130 – 170 GPa[20] and ν_{a-C} = 0.2) and find

that $E^* \approx 101 - 124$ GPa. With $F_N = 400$ nN and $R = 10$ nm, we arrive at $p_0 \approx 20–23$ GPa. Conversely, for the Si tip we estimated $p_0 \approx 10$ GPa based on $R = 10$ nm, $E^* \approx 100$ GPa and $F_N = 100$ nN[15] indicating a clear difference in the critical pressures that govern the low-to-high friction transition in diamond and silicon tip FFM experiments. Note, while applying the Hertz formula is a rough approximation and assuming certain elastic moduli for the materials are subject to considerable uncertainties, we believe that trends are reasonably captured.

Previously, atomistic simulations were performed to explore the shear response between epitaxial graphene and the SiO_2 surface layer of the Si tip. They revealed that the step-like increase in shear stress is directly related to the formation of chemical bonds between the graphene layer and the oxygen or silicon atoms in the silicon oxide as well as the intermittent formation of a single diamond layer.[15]

Due to the sudden increase in the slope of the friction force curve with respect to the normal force, it can be hypothesized that the pressure exerted by the diamond tip also causes the formation of a single diamond layer (i.e., sp^2-to-sp^3 rehybridization of graphene, analogous to the transformation caused by the silicon tip) and the bonding of this layer to an a-C layer covering the diamond tip. In the following section, we confirm this hypothesis using DFTB simulations.

2.2. Simulations

2.2.1. Sliding Regimes

Molecular dynamics (MD) simulations were conducted to model the sliding interaction between a passivated a-C slab (representing the a-C overlayer on the diamond tip) and an epitaxial graphene sheet on SiC(0001). To account for local variations in the a-C overlayer on the diamond tip, four different structural a-C configurations were prepared to simulate diverse atomic arrangements, following the same approach used for the SiO_2 slabs in ref. [[15]]. The simulations aim to investigate the pressure dependence of the shear behavior and the possible subsequent structural changes at the interface between the diamond tip and the epitaxial graphene.

Figure 2 displays representative snapshots captured during the final 0.1 ns of a 0.2 ns simulation period. The velocity profiles (green curves in Figure 2) are superimposed in order to mark the spatial region that accommodates the applied shear. The a-C slab simulations are compared with the SiO_2 slab results from ref. [[15]] – see the lowest row in Figure 2. By applying a predefined normal pressure (P) between 5 and 22.5 GPa, the simulations systematically evaluate the structural evolution at the interface between the amorphous layers and graphene/SiC(0001) during sliding at a temperature of 300 K and a velocity of 100 m s^{-1}. While Figure 2 reports representative results from one of the four trajectories, **Figure 3a** displays the mean steady state shear stress of all four runs as a function of applied normal pressure (green and black symbols for a-C as well as blue and red symbols for SiO_2). An inspection of Figures 2 and 3 reveals that the tribological systems with the a-C and the SiO_2 slabs exhibited distinct sliding regimes, with different characteristics emerging across the examined normal pressure range.

Regime I. For normal pressure less than 12.5 GPa, no chemical bonds are formed between the a-C and graphene, nor between graphene and the carbon interface layer (IFL) on top of SiC. In this regime, the shear plane is located between H/OH-terminated a-C and graphene. Similarly, for the SiO_2 slab, no chemical bonds form between the interfaces for normal pressures below 10 GPa, and the shear plane is located between SiO_2 and graphene. Consequently, the shear stress (τ) in both cases remains small (τ <0.061 GPa for SiO_2 and τ <0.045 for a-C, see Figure 3a) and the resulting friction coefficients (μ) ($\mu = \frac{\tau}{p} = 0.008 < 0.01$ for SiO_2; $\mu = \frac{\tau}{p} = 0.006 < 0.01$ for a-C) indicate superlubricious sliding.

Regime II. As the normal pressure reaches 12.5 GPa, C—C bonds form between a-C and graphene, as well as between graphene and the IFL, marking the onset of a new sliding regime. This observation aligns with Bundy et al.'s findings that graphite transitions to diamond at pressures of ≈13 GPa.[21] In this regime, the shear plane remains in the gap between a-C and graphene, gradually shifting closer to the graphene layer. In addition, the passivating H and OH groups transfer from the a-C tip to graphene, and some ether functional groups form on graphene, which bond back with the a-C surface at this pressure range. The SiO_2 tip enters a similar regime at a normal pressure of 10 GPa, where SiO_2-graphene and graphene-IFL bond formation begins. In these cases, however, the shear plane moves upwards due to plastic events in SiO_2 in addition to the sliding at the graphene-SiO_2 interface.

Regime III. As the normal pressure increases to 15 GPa, the number of C—C bonds between the terminated a-C and graphene and between graphene and the IFL increases. The increased bonding between graphene and IFL causes them to be dragged along with the a-C slab, resulting in a new sliding regime where the shear plane is predominantly located between the IFL and SiC. This regime persists up to our maximum normal pressure of 22.5 GPa. Notably, at this pressure range, the terminating H and OH groups mostly migrate away from the graphene and bond with carbon atoms deeper within the a-C, playing a minor role at the a-C/graphene interface. Similarly, at a normal pressure of 15 GPa for the SiO_2 slab, a behavior comparable to that observed with a-C was noted, with an almost full connection between graphene and the IFL. Moreover, numerous bonds (O—C and Si—C) formed between SiO_2 and graphene, resulting in the emergence of sliding regime III, where the shear plane now shifts fully upward into silicon oxide. In addition, this regime continued for normal pressures up to 22.5 GPa.

The different shear plane locations observed in the a-C and SiO_2 simulations can be attributed to the different mechanical properties of both materials. The strong covalent C—C bonds in a-C contribute to its high hardness and resistance to deformation, allowing the material to maintain its rigidity. This rigidity, combined with strong bonding between a-C and graphene, ensures that the graphene/IFL group remains firmly attached to the a-C, thereby positioning the shear plane at the interface between the IFL and SiC. In contrast, the SiO_2 structure, which involves Si—O bonds, is relatively soft and can form strong Si—C and O—C bonds with the graphene layer (which has evolved to a single layer of diamond).[22] This softer nature along with the strong bond formation at the interface, causes the shear plane to shift upward into the silicon oxide layer under increasing normal pressures.

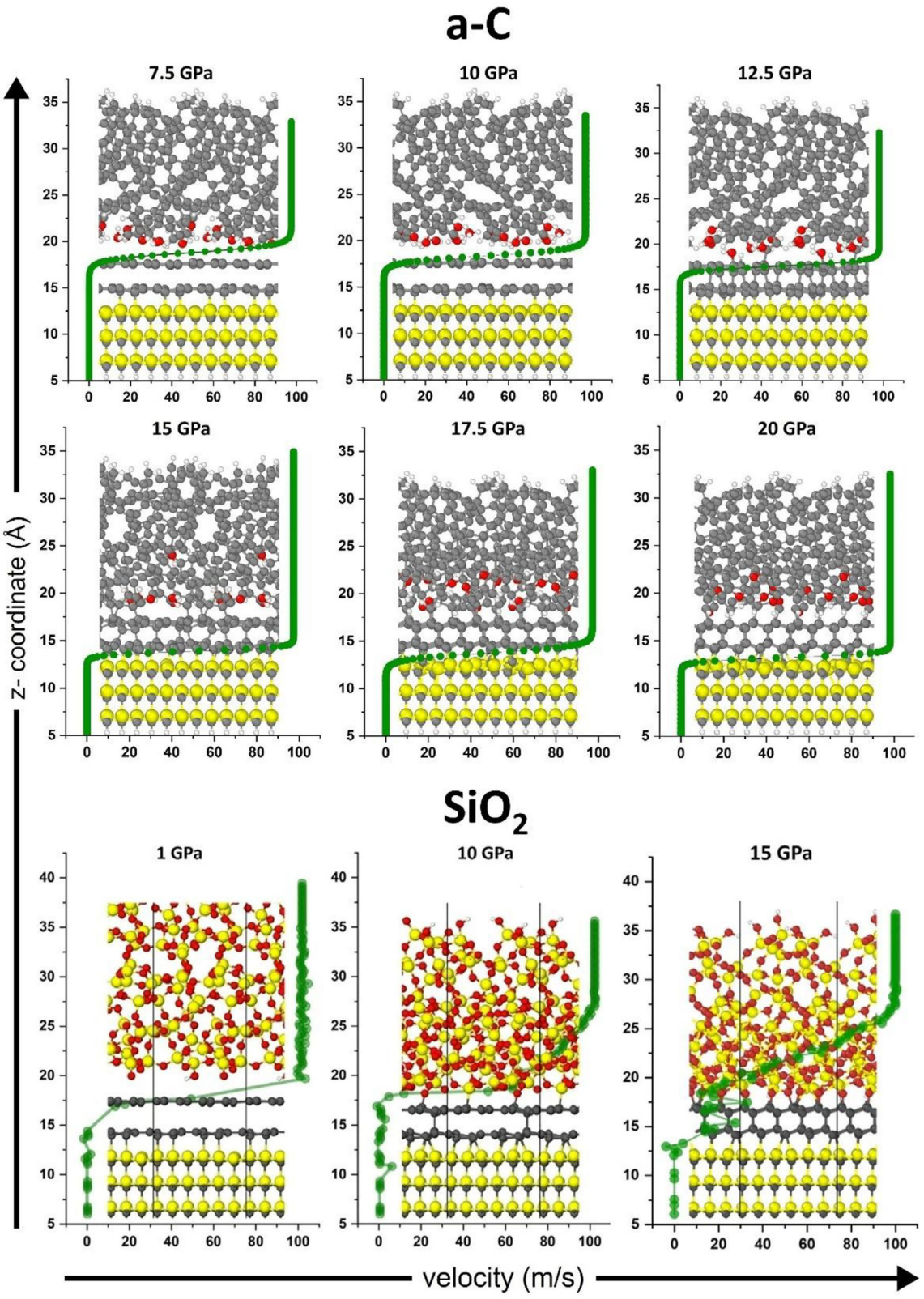

Figure 2. Atomistic simulation of a-C and SiO_2 slabs sliding on epitaxial graphene/SiC(0001) with a velocity of 100 m s^{-1} and at a temperature of 300 K. Representative snapshots that were captured during the final 0.1 ns of a 0.2 ns simulation period. Colors distinguish elements: yellow for silicon, red for oxygen, gray for carbon, and white for hydrogen. Sticks between spheres denote chemical bonds. The green data points show the sliding velocity as a function of the normal coordinate (*z*) and mark the location of the shear plane.

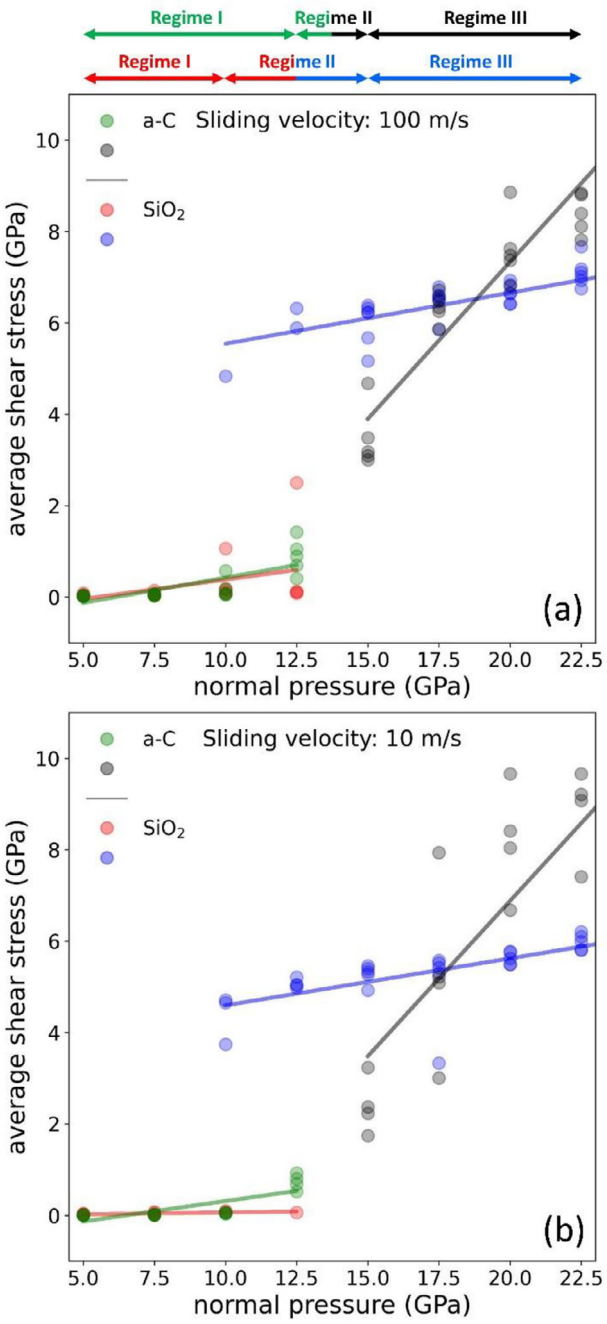

Figure 3. Shear stress response of a-C and SiO_2 on graphene/SiC as a function of normal pressure at 300 K for two sliding velocities: a) 100 and b) 10 m s^{-1}. Each data point represents the mean value from independent MD simulations. Arrows at the top of panel (a) indicate the approximate normal-pressure ranges associated with distinct sliding regimes: green and black arrows for a-C, and red and blue arrows for SiO_2. For a-C, green symbols denote low-friction configurations with no or few C—C bonds formed between the tip and graphene or between graphene and the IFL, whereas black symbols correspond to high-friction cases with an increasing number of C—C bonds at these interfaces. For SiO_2, red symbols indicate the absence of chemical bonding between the tip and graphene, while blue symbols correspond to cases where at least one C—Si or C—O bond forms at the interface.

The impact of bond formation on shear stress across different interfaces will be explored in detail in the next section.

In the following, we discuss the variation of shear stress for the a-C and SiO_2 systems under different normal pressures (Figure 3a). Our results show that the shear stress for the a-C significantly increases with pressure. At lower contact pressures, the a-C demonstrates smooth sliding over graphene with minor shear stress due to the absence of chemical bonding (see 7.5 and 10 GPa snapshots in Figure 2). However, as the contact pressure increases, the initiation of C—C bonding between a-C and graphene, as well as between graphene and the IFL, leads to higher shear stress driven by increased resistance to sliding (approaching a shear stress of ≈8 GPa for the highest normal pressure). Also, the SiO_2 slab generally exhibits an increase in shear stress with contact pressure, characterized by a significant step-like increase toward a shear stress of ≈6 GPa in the normal pressure range between 10 and 12.5 GPa. Remarkably, this transition pressure range is significantly lower for the SiO_2 than for the a-C case (compare red and black symbols in Figure 3a).

2.2.2. Influence of Sliding Velocity

The velocity of the FFM tips is orders of magnitude smaller than the sliding velocities in the DFTB simulations. Therefore, we performed an additional simulation campaign at a sliding velocity of 10 m s^{-1} to assess the effect of the velocity of the amorphous counter slabs (Figure 3b). For both the a-C and SiO_2 counter bodies, the shear stress values at 10 m s^{-1} are close to those at 100 m s^{-1} across the range of normal pressures (5 to 22.5 GPa) and at a temperature of 300 K, indicating only a marginal influence of sliding velocity. For both amorphous counter materials, the onset of the transition between regimes I and II seems to shift to smaller pressures when the sliding velocity is reduced. While sliding velocity has an impact on the transition pressures, its effect on the shear stress plateau at high normal pressures is rather weak. See Figures S3 and S4 of the SI for similar assessment of the temperature dependence of the shear stress.

Based on Figure 3b, we can roughly estimate the normal pressures that induce a high shear stress response. For SiO_2, high shear stress occurs already at ≈10 GPa, whereas for a-C, shear stress exceeds 1 GPa only at normal pressures above ≈15 GPa. These estimates are approximate and could easily have an uncertainty of ±1 GPa. Nevertheless, they align well with the experimental estimates of 10 GPa for SiO_2 and 20–23 GPa for a-C.

2.2.3. Evolution of Total Density, Oxygen Density, and Velocity Profile

To further explore interfacial interactions, shear behavior, and material deformation, we calculated the total density, oxygen density, and velocity profiles under different normal pressures (representing the various sliding regimes) at different times during the simulations. For each normal pressure, the data in **Figure 4** is derived from the same sample as in Figure 2. The selected trajectory highlights detailed structural and velocity characteristics, capturing subtle features. To confirm the representativeness of our choice, we provide an average over all four independent runs in the SI (Figure S5). This averaged data validates the robustness

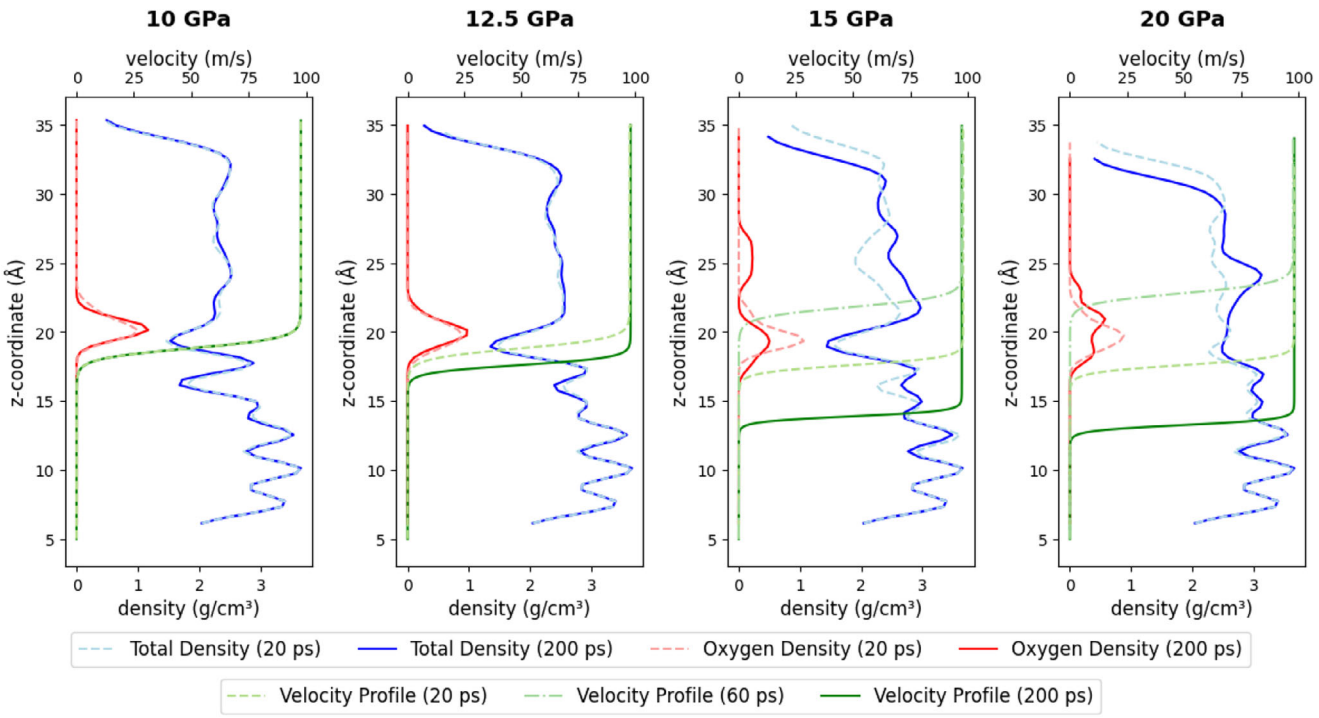

Figure 4. Velocity profiles and density distributions of the a-C/Graphene/SiC system under varying normal pressures (10, 12.5, 15, and 20 GPa) as a function of z– coordinate. Total density (blue lines) and oxygen density (red lines) at 20 ps (dashed lines) and 200 ps (solid lines) illustrate the structural evolution of the system. Velocity profiles at 20 ps (green dashed line), 60 ps (green dash-dot line), and 200 ps (solid green line) highlight the location of the shear plane during this evolution. At higher pressures, intermediate chemical mixing occurs in the a-C, leading to its densification accompanied by the migration of oxygen atoms into the bulk a-C region.

of the trends described in the main text but obscures finer details that are critical for interpreting specific interfacial behaviors.

We start with a description of the 10 GPa results. Initially, the total density (dashed blue curve) shows the expected oscillations of the crystalline SiC (including the IFL bonded to the SiC) for z <15 Å. Graphene is represented by the peak at z = 17 Å, while a-C gives rise to a structureless density plateau with 2.2 g cm^{-3} for z ≥ 20 Å. The oxygen atoms are located at z = 20 Å, visible as a pronounced peak in the initial oxygen density (dashed red curve). The initial velocity profile (dashed green curve) jumps from 0 to 100 m s^{-1} in a narrow region around z = 18 Å, indicating sliding of the H/OH-passivated a-C over epitaxial graphene. This behavior is conserved during the whole simulation, so that the densities and the velocity profile at the beginning and the end of the trajectories are almost identical (compare dashed and solid lines in Figure 4).

Also, in the 12.5 GPa case, the density profiles did not exhibit any significant changes during the simulation. However, in the initial total density, the location of graphene is lower compared to the 10 GPa case, because bonding between graphene and the IFL starts early in the simulation. The shear plane shifts downward by ≈1 Å within the first 60 ps (compare dashed and dot-dashed green curves), reflecting the onset of bonding of a-C to graphene accompanied by slip events of graphene against the IFL.

As the pressure increases further to 15 and 20 GPa, the depletion of passivating hydroxyl groups at the a-C/graphene interface results in cold welding between a-C and the graphene layer. This leads to substantial chemical mixing of the a-C that drives densification (with local peaks in the a-C total density reaching almost 3 g cm^{-3}) and migration of oxygen atoms deeper into the a-C layer (red solid curves). The shear plane moves temporarily into the a-C bulk; see the dash-dotted green curve for the velocity profile at 60 ps. The chemical mixing stops within 0.2 ns.

This behavior reflects localized, shear-induced plasticity within the a-C layer, involving irreversible atomic rearrangements and densification. Additional insight into this mechanism was gained by analyzing the evolution of carbon hybridization during sliding at 20 GPa, which shows a transient increase in sp^3 content during the initial 100 ps, stabilizing as sliding progresses (see Figure S6 of the SI). In this high-pressure regime, a shear-induced sp^2-to-sp^3 rehybridization occurs within the a-C tip. This transformation results from plastic flow, with the steady-state structure defined by density and hybridization ratio, and governed by the applied normal load, consistent with Moras et al.[23] The observed densification agrees with their report that shear-induced a-C structures at 20 GPa exceed our initial density of 2.2 g cm^{-3}. Although the nature of rehybridization depends on the initial density, the final structure formed under sustained shear is determined solely by the normal load and is independent of the initial a-C structure. This trend was consistently observed across four independent simulations, further supporting the presence of structural plasticity.

As indicated by the solid green velocity profile in Figure 4, the shear plane shifted toward the interface between the IFL and the SiC substrate. The total density profiles in Figure 4 provide additional evidence of structural transformation in the

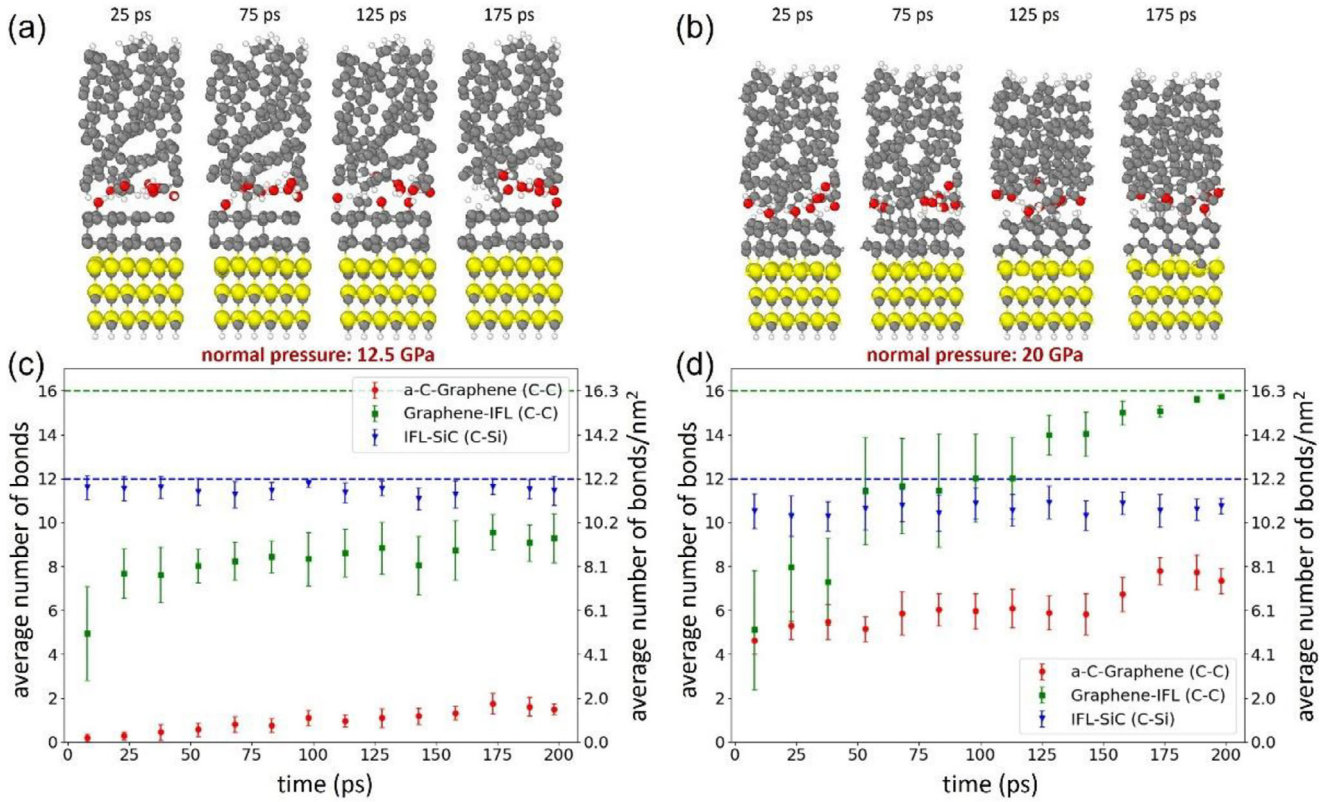

Figure 5. Evolution of a-C/Graphene/SiC configurations and corresponding average number of C—C and C—Si bonds over time for two normal pressures, 12.5 GPa (left column) and 20 GPa (right column), representing regime II and regime III of sliding, respectively. The top panels a and b display snapshots of the atomic configurations at different time intervals (25, 75, 125, and 175 ps). The bottom panels c and d illustrate interactions at three interfaces by reporting the average number of C—C and C—Si bonds: a-C/graphene (red disks), graphene/IFL (green squares), and IFL/SiC (blue triangles). Blue and green dashed lines at bond counts of 12 and 16 represent the maximum possible number of C—Si and C—C bonds at the IFL/SiC and graphene/IFL interfaces, respectively. The right-hand *y*-axis presents the normalized number of C—C and C—Si bonds per square nanometer. Each average represents the mean number of bonds over a 14 ps simulation period, providing a representative value for that time period. The results were then averaged across the four samples to obtain a reliable estimate of the mean bond count.

graphene/IFL zone. At the lowest pressure (10 GPa), the total density profile in the graphene region shows two distinct peaks, corresponding to a clear separation between graphene and IFL. However, as the pressure increases, these peaks converge to a bimodal peak. This reflects the increased chemical bonding between graphene and IFL, finally forming a single layer of diamond (see Figure 2).

2.2.4. Bonding Dynamics, System Configuration Evolution, and Shear Stress

To better understand the evolution of the mechanical strength and stability of the various interfaces, we analyzed the interfacial bond formation over time. It is important to note that no new bond formation occurred at any interface during sliding regime I. Consequently, this analysis focuses on sliding regimes II and III, where C—C and C—Si bond formation was observed. **Figure 5** shows the typical time evolution of a-C/Graphene/SiC configurations (panel (a) for 12.5 GPa and panel (b) for 20 GPa normal pressure) for these two regimes. Panels (c) and (d) report the corresponding average numbers of C—C and C—Si bonds over a 0.2 ns sliding period of the a-C overlayer across the epitaxial graphene on SiC.

In regime II (Figure 5a), the applied normal pressure is sufficient to initiate the formation of new C—C bonds between a-C and graphene. However, the average number of these bonds remains low throughout this regime, ranging from 0 to ≈2 bonds nm^{-2} (Figure 5c), indicating limited bonding and interaction between these two layers. Conversely, in regime III (Figure 5b) the number of bonds between a-C and graphene increases to 8 bonds nm^{-2}. Apparently, the densification of the a-C brings more carbon atoms into contact with graphene. This results in greater frictional resistance, leading to an increase in shear stress (Figure 3a). Even with just 8 C—C bonds nm^{-2}, the a-C layer can effectively cold weld with the graphene/IFL single-layer diamond, highlighting the critical role of these bonds in enhancing the overall mechanical behavior under elevated pressure conditions.

At the graphene/IFL interface, the C—C bond count shows an even more pronounced dependence on the normal pressure. In regime II (see Figure 5c), the bond count starts at ≈5 bonds nm^{-2} and gradually increases to ≈9 bonds nm^{-2} over time, which is significantly below the possible maximum of 16.3 bonds nm^{-2}

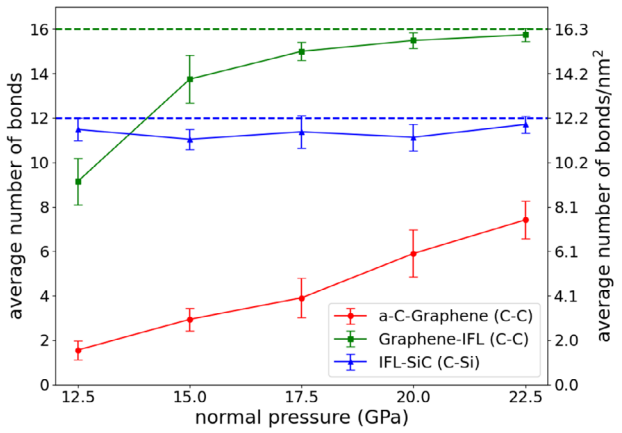

Figure 6. Average number of bonds as a function of normal pressure for three different interfaces: a-C/graphene (C—C), graphene/IFL (C—C), and IFL/SiC (C—Si), based on data from the last 50 ps of the simulations. The dashed lines indicate the possible maximum number of bonds for the graphene/IFL (16 bonds, green) and IFL/SiC (12 bonds, blue) interfaces. The secondary y-axis on the right shows the normalized bond count per square nanometer.

(indicated by the green dashed line). This gradual increase indicates the activation of additional bonding sites between graphene and the IFL during sliding. In regime III (Figure 5d), the bond count between graphene and the IFL rises further, approaching the maximum possible count of 16 bonds nm^{-2}. This complete bond formation at the graphene/IFL interface suggests a strong structural transformation resulting in the formation of a single layer of diamond.

Finally, we consider the number of bonds at the IFL/SiC interface. In regime II (Figure 5c), the bond count remains consistently high, around the theoretical maximum of 12 bonds nm^{-2}. Occasional fluctuations can be attributed to slip events between the IFL and the SiC substrate. In regime III (Figure 5d), a different scenario unfolds. The increased bonding between graphene and the IFL promotes the formation of the single-layer diamond, whose cold welding with a-C causes the IFL to slip at a sliding velocity of 100 m s^{-1} over the SiC surface. This results in the successive breaking and reformation of C—Si bonds at the IFL/SiC interface, as reflected in the bond count fluctuation between 10 and 12 bonds nm^{-2} (Figure 5d).

To understand how interfacial interactions influence changes in shear stress and mechanical stability, we studied the effect of varying normal pressures on the final bond density at different interfaces. **Figure 6** displays the average number of C—C bonds at the a-C/graphene and graphene/IFL interface as well as the average number of C—Si bonds at the IFL/SiC interface as a function of normal pressure. At the a-C/graphene interface, the number of C—C bonds gradually increases with the normal pressure, from ≈2 bonds nm^{-2} at 12.5 GPa to ≈7 bonds nm^{-2} at 22.5 GPa. Note that this increase in bond formation correlates directly with the rise in shear stress observed at this interface (Figure 3a). As more C—C bonds form between the a-C and graphene layers, the interfacial adhesion is enhanced, leading to increased frictional resistance and, consequently, higher shear stress.

For the graphene/IFL interface, the number of C—C bonds increases rapidly as the normal pressure rises, approaching the possible maximum of 16 bonds nm^{-2}. This indicates that at higher pressures, this interface achieves near-complete bond saturation, which also contributes to the overall increase in shear stress and mechanical stability. In contrast, the IFL/SiC interface exhibits remarkable stability across all normal pressures, with the number of C—Si bonds fluctuating slightly below the possible maximum of 12 bonds nm^{-2}. This consistent bond count, despite the dynamic adjustments observed earlier, suggests that the interface is able to maintain its structural integrity even under increased pressures. This stability implies that the IFL/SiC interface plays a supporting role in maintaining mechanical stability, without significantly impacting the variations in shear stress observed at other interfaces. Consequently, while the a-C/graphene and graphene/IFL interfaces show a direct correlation between bond density and shear stress, the IFL/SiC interface provides a stable foundation that adapts to the shifting shear plane, accommodating bond breaking and reformation activities at this interface without compromising its overall bond density.

2.2.5. Structure of the Epitaxial Graphene after Sliding

On the one hand, the simulations showed extensive bonding between the IFL and graphene as well as between graphene and a-C under regime II and III conditions resulting in complete cold welding of the entire tribosystem (consisting now of a SiC/single-layer diamond/a-C cold-welded layer system). On the other hand, overview images across the site of previously performed high-load series (such as the one shown in Figure S1c of the SI) revealed that there was no local change in friction and no local change in topography, i.e., there was no trace of the single-layer diamond or adatoms on the graphene terraces. This opens the question of whether the simulations also predict a recovery of the graphene to its original state after the sliding simulations. To elucidate the structure of the epitaxial graphene after tip retraction, we conducted additional simulations where the a-C layer was lifted upwards after the initial 0.2 ns sliding period. During these simulations, the a-C slab was slid along the x-direction at a x-velocity of 100 m s^{-1} while being gradually retracted in the normal direction at a z-velocity of 10 m s^{-1}. **Figure 7** illustrates this process with a series of snapshots from the 0.2 ns lift-off simulation for normal pressures of 15 and 17.5 GPa.

At 15 GPa, the snapshots in the top row of Figure 7 reveal the gradual detachment of the a-C from the graphene interface during the lift-off process. Initially, one oxygen and one hydrogen atom are bonded to the single-layer diamond and a few C—C bonds bridge the gap between the single-layer diamond and the a-C (Figure 7a). As the retraction of the a-C slab progresses, these C—C bonds and a series of C—C bonds in the single-layer diamond break (Figure 7b). Simultaneously, a free CO molecule forms, while a hydroxyl group, a CH group, and a hydrogen atom remain attached to the graphene surface. In principle, the OH group and one of the hydrogen atoms could combine to form a water molecule, while the remaining carbon adatom could react with another oxygen atom on the surface of the tip to produce a second CO molecule. Given that the experimental tip is significantly larger than the simulated one and operates at a much lower sliding speed, the reaction of the hydrogen and carbon atoms on the graphene surface with the tip, followed by their removal, is

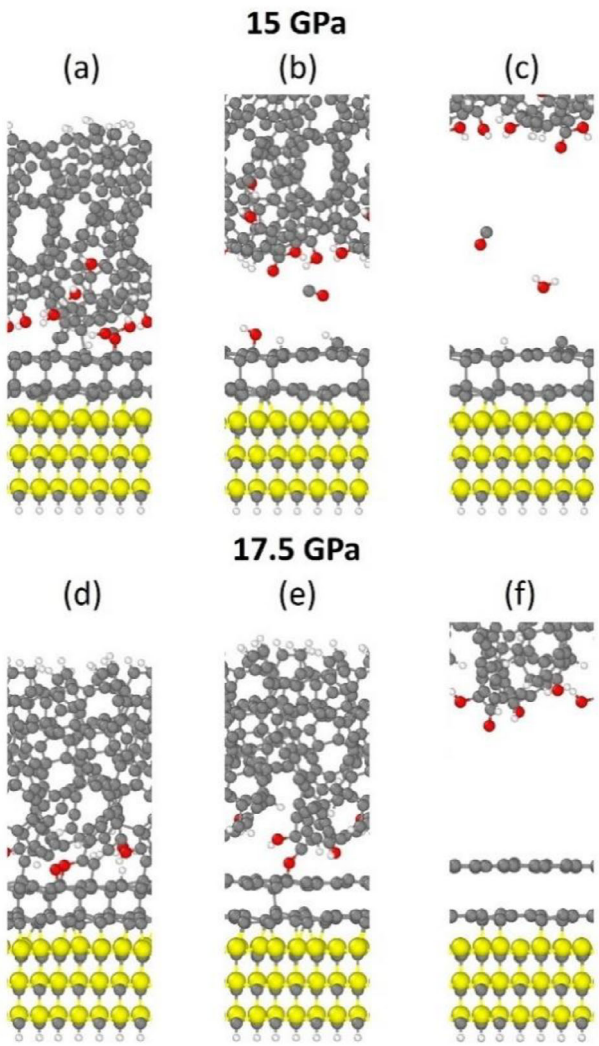

Figure 7. Snapshots from the lift-off simulations of the a-C tip following 0.2 ns of simulations at normal pressures of 15 GPa (top row) and 17.5 GPa (bottom row). The frames, arranged sequentially from left to right, illustrate key stages of the structural evolution during the lift-off phase. The images highlight the restoration of interlayer distances and changes in interfacial configurations, providing insights into the system's behavior during retraction.

highly probable. This process would ultimately lead to the opening of the remaining single-layer diamond bonds, allowing the graphene to recover its structure and return to its initial distance from the IFL.

To further analyze this behavior, we performed density functional theory (DFT) calculations to evaluate the energetics of the desorption of H and OH from the graphene surface and the subsequent formation of a water molecule in the tribological gap (Figure 7c). The energy difference between the system configurations in Figure 7b and Figure 7c is negative (−0.138 eV), indicating that the formation of a water molecule is energetically favorable compared to having H and OH adsorbed on the surface. This result highlights the thermodynamic preference for water formation and its detachment from the graphene interface. With the same reasoning, one can argue that the remaining H and C adatoms will leave the graphene, resulting in an incomplete single-layer diamond free of adatoms. Finally, heating this system to 500 K shows that the graphene fully detaches from the IFL.

At 17.5 GPa, the situation is even clearer, as the lift-off proceeds through the breaking of various C—C and C—O bonds between the graphene and the a-C layer (see the evolution from Figure 7d,e). This process is accompanied by the dissociation of nearly all interplane bonds in the single-layer diamond structure. After the final ether bridge breaks (between Figure 7e,f), the ideal epitaxial graphene spontaneously reforms. The behavior observed in these lift-off simulations suggests that the graphene interface is capable of returning to its pre-sliding configuration, demonstrating the resilience of the system under moderate pressure and thermal conditions.

2.2.6. Effect of the IFL Mobility

As shown in Figure 2, during sliding regime III, the single-layer diamond (formed, for example, at 20 GPa) is dragged along with the a-C slab. However, this scenario is unlikely in experiments since the graphene flakes are micron-sized and pushing them over the SiC surface would require unrealistically large forces. In this context, the periodic boundary conditions in the simulations translate into an infinite array of tips capable of shifting entire graphene flakes—an artifact of the simulation setup.

To address this issue, we took the samples from normal pressures 15 and 20 GPa simulations after 0.2 ns and made a minor modification to the protocol. Specifically, we froze the x-position of the IFL atoms to ensure that the single-layer diamond remained anchored to the SiC substrate. This adjustment mitigated the artifact caused by periodicity in the simulation setup. We then ran the sliding simulation for an additional 0.2 ns.

The resulting velocity profiles, shown in **Figure 8**, illustrate a shift in the shear plane location into the a-C region for both normal pressures. The fixed IFL layer, combined with multiple (a-C)C—C(graphene) bonds that anchor the a-C atoms near the graphene layer to the interface, causes the shear plane to relocate upward into the a-C layer. At 15 GPa, the shear plane is located in the a-C, close to the graphene layer, while at 20 GPa, the shear plane is located deeper within the a-C layer. The average steady shear stress increased significantly with the modified setup, rising from $\tau = 3.5$ GPa to $\tau = 7.9$ GPa for normal pressure 15 GPa and from $\tau = 7.6$ GPa to $\tau = 12.3$ GPa for normal pressure 20 GPa. This result aligns with prior studies on the plasticity of a-C,[24] showing that the interface sets a lower bound on the flow stress, with shear stress increasing linearly above 8 GPa, indicating enhanced resistance to shear under compression.

3. Conclusion

The sliding interaction between an a-C-covered diamond tip and an epitaxial graphene layer on SiC(0001) was compared with the sliding behavior of a SiO_2-covered Si tip. Experimental FFM measurements and MD simulations using the DFTB method were conducted to explore the tribological properties of these material systems under various normal pressures and temperatures.

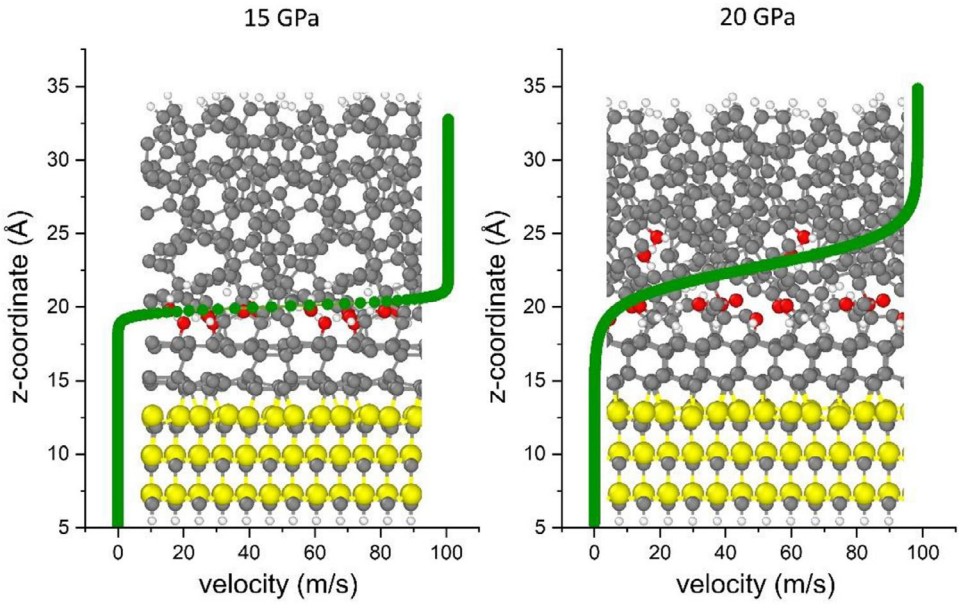

Figure 8. Velocity profile illustrating the shear plane shift into the a-C region after freezing the *x*-position of the IFL atoms during the modified 20 GPa simulation.

The experiments with the Si tip exhibited an initial linear low-friction regime up to a normal force of 80 nN, followed by a rapid increase in friction. High friction values generally increased with pressure but showed significant scatter, occasionally returning to the low-friction regime. For the diamond tip, a low-friction regime with fluctuating friction force was observed for normal forces up to 400 nN, followed by a linear-like increase in friction force. For both tip materials, the threshold for the high friction regime shifts to higher normal forces when the measurements are repeated (180 nN for Si and 500 nN for diamond), indicating blunting of the tips. Using the initial tip radii (estimated 10 nm from TEM imaging) in Hertz contact mechanics theory results in a clear ranking of the threshold pressures (≈10 GPa for Si and ≈20 GPa for diamond), aligning with an accompanying simulation study.

Our MD simulations identified distinct sliding regimes, each characterized by unique bond formation dynamics and shear plane locations. At low pressures, no chemical bonds formed, and the shear plane was located between the tip and graphene (Regime I: P<12.5 GPa for a-C, P < 10 GPa for SiO_2). As the pressure increased, a-C–Graphene and SiO_2–Graphene bond formation commenced, while the shear plane remained between the tips and graphene (Regime II: 12.5 GPa ≤ P < 15 GPa for a-C, 10 GPa ≤ P < 15 GPa for SiO_2). At higher pressures, the behavior of the two materials diverged. For a-C, tip-graphene bond formation was accelerated, with the shear plane primarily located between the IFL and SiC. In contrast, for SiO_2, the shear plane shifted upward into silicon oxide (Regime III: 15 GPa ≤ P ≤ 22.5 GPa for both a-C and SiO_2). It is worth noting that the different locations of the shear interface in the two materials in Regime III also conform to the different pressure dependences of their yield stress for plastic flow. This highlights the distinct behaviors of a-C and SiO_2 in frictional interactions with graphene, driven by their material properties and bonding mechanisms. The a-C layer exhibits high plastic yield stress and rigidity, while SiO_2 is softer and allows for easier plastic flow.

These differences in mechanical strength of the two overlayer materials become more pronounced with increasing pressures: pressure-induced densification of a-C (although countered by shear deformation[23]) causes an increase in the yield shear stress.[24] In contrast, yield stress decreases with hydrostatic pressure in amorphous silicon oxide, at least for pressure lower than ≈10 GPa,[25] thus favoring plastic deformation of amorphous SiO_2.

Finally, this results in different shear plane locations and frictional responses for the two simulated tip material systems under similar pressure conditions. However, we expect the location of the shear plane to depend on the lateral size of the graphene flakes on the SiC. Most likely, for large enough graphene patches the high-pressure experimental shear zone shifts from its location between SiC and IFL into the a-C overlayer, since the lateral shear resistance of extended graphene/IFL/SiC regions is stronger compared to the laterally more confined a-C overlayer as confirmed by our additional atomistic simulations with an IFL that was pinned to resist sliding.

There is one last important point to make. The simulations showed that increased pressure leads to a strong increase of interlayer bonding resulting in a single layer of diamond that cold-welds with the a-C or SiO_2. However, the experiments provided no evidence of such an altered bonding situation after the tip was withdrawn, suggesting that the single-layer diamond is a transient structure. Indeed, additional post-sliding lift-off simulations revealed that the graphene layer could recover its original structure, demonstrating its ability to retain structural integrity even after transformation by high pressures. This reversible sp^2-to-sp^3 transition appears to be specific to the monolayer nature of epitaxial graphene. Riedo and coworkers[26,27] showed in their seminal work that already

an AFM indentation of one graphene sheet on the IFL results in a stiffening of the system that is compatible with a single layer of diamond (diamene) and that low stiffness is recovered upon retraction of the AFM tip. Interestingly, this behavior was not observed in multilayer graphene films due to stacking constraints.[26,27] Remarkably, these authors estimated the transition pressure for diamene formation to be ≈10 GPa in agreement with the pressure range found in our study. This suggests that mainly pressure-induced mechanochemistry drives the transition. Additional shear could merely facilitate the lateral movement of the graphene layers to achieve the correct stacking position that enables the transformation. Interestingly, our study reveals different transition pressures for different tip materials. In the case of Si tips (covered with SiO_2), the transition sets in at roughly 10 GPa, while epitaxial graphene under diamond tips (covered with a-C) requires even higher normal pressure; the simulations indicate a threshold at ≈15 GPa, while our rough experimental estimates are even a couple GPa higher. We believe that the difference between SiO_2 and a-C is triggered by the different chemical reactivities of both materials. Amorphous silicon oxide is less flexible in local stochiometry and therefore is less prone to self-passivation than a-C during plastic deformation.

4. Experimental Section

Experiment: The friction between epitaxial graphene on SiC(0001) and a diamond tip was measured using FFM. The lateral force acting on the tip as it slides over the graphene at different normal forces was recorded. The experimental procedures for the AFM experiments were described.[15] Briefly, the graphene/SiC(0001) samples were grown by thermal decomposition and purified by annealing in ultra-high vacuum (UHV) prior to the experiments.[28] Lateral forces were recorded in UHV by scanning the FFM tip in contact with atomically flat regions of monolayer graphene and measuring the torsion of the FFM cantilever caused by the lateral force. Friction was quantified as the mean value of lateral forces for scan areas that were large compared to the atomistic SiC(0001) surface structure. A diamond tip (Nanosensors – Adama Innovations) was used with an estimated initial radius of 10 nm (see transmission electron microscopy in Figure S7 of the SI). The results of this FFM study would be compared to the already published FFM experiments that used a silicon tip with a similar radius.[15]

Simulation: MD simulations were conducted using the DFTB method within the framework of the ATOMISTICA software suite.[29] The substrate consisted of graphene and 6 layers of SiC(0001) structure with dimensions $1.07 \times 0.92 \times 6.0\ nm^3$.

An a-C counter surface was designed to conform to these dimensions, with a density of 2.2 g cm^{-3} and 163 carbon atoms, using the ASE package[30] and the MatSciPy library.[31] The a-C structure was obtained by solidifying molten a-C under periodic boundary conditions (PBC) applied along all three Cartesian axes. Initially, the system was relaxed to avoid unfavorable atomic configurations. The system was then heated to 2000 K for 25 ps, allowing the atoms to move freely and transition into a molten state. After reaching 2000 K, the system underwent relaxation to equilibrate the atomic configuration at this temperature. Following this, the system was rapidly quenched by decreasing the temperature from 2000 to 300 K over a 25 ps period. Finally, the system was relaxed at 300 K to allow for further equilibration, ensuring a stable atomic configuration at room temperature. Throughout these steps, the system was maintained under constant volume with PBC.

Subsequently, the PBC along the z-direction was removed, creating two free surfaces (an upper and a lower one). The undercoordinated carbon atoms on the upper surface of the a-C were passivated with hydrogen atoms. The top atoms of the a-C slab within a thickness of 0.5 nm, as well as a 0.5 nm bottom layer of the graphene/SiC slab, were maintained rigid. The lower surface of the a-C slab experienced dissociative chemisorption of eight water molecules that were introduced during pressure equilibration, leading to surface passivation by hydrogen atoms and hydroxyl groups. While the passivation composition, coverage, or chemical termination were not systematically varied in the current simulations, these four different samples represent a statistical distribution of local passivation environments (for instance, hydrogenated or hydroxylated sp^2 or sp^3 sites with different neighborhoods) and therefore the variation of threshold pressure with local chemistry is roughly captured. For a detailed description of the passivating functions involved, the reader is referred to Figure S8 of the SI.

Given the computational cost and system size constraints of DFTB simulations, particularly under sliding conditions, a fixed atom count was maintained and lateral dimensions across all simulations. The thickness of the a-C model influences the overall stiffness of the tribological system and could thus affect the measured shear stress, particularly in the low-friction regime. Reichenbach et al. showed that varying the thickness of diamond-like carbon films by ≈30 nm leads to only minor changes in shear stress (0.1–0.3 GPa).[32] This magnitude of variation was significantly smaller than the shear stress difference between the low (passivated) and high (interfacial bond) friction regimes, which is the central focus of our study. Therefore, the key frictional trends reported here are largely independent of film thickness. A systematic variation of a-C thickness or structure was not performed, since accounting for the full stiffness of the FFM system—necessary for a quantitative comparison—was beyond the scope of this study.

Detailed simulation parameters for the SiO_2 counter surface were described.[15] Briefly, the amorphous SiO_2 slabs were generated by quenching a bulk silica melt and cleaving it along one Cartesian axis to expose free surfaces. After structural relaxation, dangling bonds on oxygen and silicon atoms were passivated with hydrogen and hydroxyl groups, respectively—consistent with DFT studies of silica surface chemistry in humid environments.[33] While surface terminations might vary depending on environmental conditions and pH, this passivation scheme reflects the native oxide layer typically formed on a Si FFM tip exposed to humid air and used in UHV experiments.

During the sliding MD simulations, the Pastewka-Moser-Moseler pressure-coupling algorithm was employed.[34] The rigid a-C atoms underwent sliding motion along the *x*-axis at velocities of 10 and 100 m s^{-1}, operating under varying normal pressures ranging from 5 to 22.5 GPa, while the positions of the rigid layers of the graphene/SiC slab remained unchanged. A Langevin thermostat,[35] acting perpendicularly to the sliding direction, regulated the constant system's temperatures of 300, 500, and 1000 K. The equations of motion were integrated using the velocity Verlet algorithm[35] with a time step of 0.5 fs. To calculate the shear stress, the force components exerted along the *x*-axis on the rigid layers of the a-C were summed and then divided by the lateral area of the simulation cell. Subsequently, the calculated shear stress was averaged over the final half of the total simulation time of 0.2 ns.

To analyze the bonding behavior in the system, the number of bonds was calculated between specific atom pairs across multiple configurations over the course of the 0.2 ns simulations. Bonds were identified based on interatomic distances, using a threshold of 1.85 Å for C—C bonds and 2.2 Å for C—Si bonds. This process was applied to every configuration in the simulation, systematically evaluating all atomic pairs to determine bond counts in each frame. To visualize the results of the simulations, the output data were processed using the Ovito freeware.[36]

The mass distribution was examined by calculating the density profile along the *z*-axis of the simulation box. The simulation box was divided into discrete 0.4 Å bins along the *z*-direction, and atoms were assigned to these bins based on their z-coordinates. For each bin, the total mass of atoms was computed by summing the atomic masses of all atoms within the bin using predefined values for each atomic species. To calculate the velocity profile, the simulation box was similarly divided into layers along the *z*-direction, grouping particles within each layer. The *x*-velocities of these particles in the sliding direction were then averaged to provide a

representative velocity for each layer. The calculated velocity profile was averaged over the final half of the total simulation time.

Supporting Information

Supporting Information is available from the Wiley Online Library or from the author.

Acknowledgements

The authors acknowledge financial support by the Deutsche Forschungsgemeinschaft within the Research Unit 5099 (M.M. and M.Z.) and the Priority Program SPP 2244 "2DMP" (B.S. and R.B.). Sample preparation by Thomas Seyller (University of Technology Chemnitz) is gratefully acknowledged. Computing time was granted by the John von Neumann Institute for Computing (NIC) and provided on the supercomputer JUWELS at Jülich Supercomputing Centre (JSC) within the Project Harsh. T.K. acknowledges financial support from MEXT Leading Initiative for Excellent Young Researchers (JPMXS0320210079) and JST PRESTO (JPMJPR22A6). The authors are also grateful to Thomas Reichenbach for insightful discussions that contributed to this work. The authors thank Dr. Marcus Koch from Leibniz-INM for helping to take the TEM images in Figure S8.

Open access funding enabled and organized by Projekt DEAL.

Conflict of Interest

The authors declare no conflict of interest.

Data Availability Statement

The data that support the findings of this study are available from the corresponding author upon reasonable request.

Keywords

friction, friction force microscopy, molecular dynamics simulations, single-layer diamond, supported graphene

Received: June 6, 2025
Revised: August 22, 2025
Published online:

[1] M. M. Van Wijk, M. Dienwiebel, J. W. M. Frenken, A. Fasolino, *Phys. Rev. B* **2013**, *88*, 235423.
[2] S. Wang, L. Y. Zhao, Y. Liu, *Comput. Methods Appl. Mech. Eng.* **2022**, *392*, 114644.
[3] S.-W. Liu, H.-P. Wang, Q. Xu, T.-B. Ma, G. Yu, C. Zhang, D. Geng, Z. Yu, S. Zhang, W. Wang, Y.-Z. Hu, H. Wang, J. Luo, *Nat. Commun.* **2017**, *8*, 14029.
[4] Z. Cheng, H. Feng, J. Sun, Z. Lu, Q. C. He, *Adv. Mater. Interfaces* **2023**, *10*, 2202062.
[5] E. Gao, B. Wu, Y. Wang, X. Jia, W. Ouyang, Z. Liu, *ACS Appl. Mater. Interfaces* **2021**, *13*, 33600.
[6] D. Berman, S. A. Deshmukh, S. K. R. S. Sankaranarayanan, A. Erdemir, A. V. Sumant, *Science* **2015**, *348*, 1118.
[7] F. B. Wu, S. J. Zhou, J. H. Ouyang, S. Q. Wang, L. Chen, *Lubricants* **2024**, *12*, 138.
[8] S. Zhang, Y. Hou, S. Li, L. Liu, Z. Zhang, X.-Q. Feng, Q. Li, *Proc. Natl. Acad. Sci. USA* **2019**, *116*, 24452.
[9] J. Li, J. Li, J. Luo, *Adv. Sci.* **2018**, *5*, 1800810.
[10] D. Berman, A. Erdemir, A. V. Sumant, *Mater. Today* **2014**, *17*, 31.
[11] S. Kawai, A. Benassi, E. Gnecco, H. Söde, R. Pawlak, X. Feng, K. Müllen, D. Passerone, C. A. Pignedoli, P. Ruffieux, R. Fasel, E. Meyer, *Science* **2016**, *351*, 957.
[12] C. Lee, Q. Li, W. Kalb, X.-Z. Liu, H. Berger, R. W. Carpick, J. Hone, *Science* **2010**, *328*, 76.
[13] X. Ge, Z. Chai, Q. Shi, Y. Liu, W. Wang, *Friction* **2023**, *11*, 1953.
[14] T. Filleter, J. L. McChesney, A. Bostwick, E. Rotenberg, K. V. Emtsev, T. Seyller, K. Horn, R. Bennewitz, *Phys. Rev. Lett.* **2009**, *102*, 086102.
[15] B. Szczefanowicz, T. Kuwahara, T. Filleter, A. Klemenz, L. Mayrhofer, R. Bennewitz, M. Moseler, *Phys. Rev. Res.* **2023**, *5*, L012049.
[16] M. Elstner, D. Porezag, G. Jungnickel, J. Elsner, M. Haugk, T. Frauenheim, S. Suhai, G. Seifert, *Phys. Rev. B* **1998**, *58*, 7260.
[17] B. Luan, M. O. Robbins, *Nature* **2005**, *435*, 929.
[18] A. Klemenz, A. Gola, M. Moseler, L. Pastewka, *Appl. Phys. Lett.* **2018**, *112*, 061601.
[19] R. Jana, D. Savio, V. L. Deringer, L. Pastewka, *Model. Simul. Mater. Sci. Eng.* **2019**, *27*, 085009.
[20] D. Schneider, B. Schultrich, *Surf. Coatings Technol.* **1998**, *98*, 962.
[21] F. P. Bundy, W. A. Bassett, M. S. Weathers, R. J. Hemley, H. U. Mao, A. F. Goncharov, *Carbon N. Y.* **1996**, *34*, 141.
[22] A. Peguiron, G. Moras, M. Walter, H. Uetsuka, L. Pastewka, M. Moseler, *Carbon N. Y.* **2016**, *98*, 474.
[23] G. Moras, A. Klemenz, T. Reichenbach, A. Gola, H. Uetsuka, M. Moseler, L. Pastewka, *Phys. Rev. Mater.* **2018**, *2*, 083601.
[24] R. Jana, J. von Lautz, S. M. Khosrownejad, W. B. Andrews, M. Moseler, L. Pastewka, *J. Phys. Mater.* **2020**, *3*, 035005.
[25] B. Mantisi, G. Kermouche, E. Barthel, A. Tanguy, *Phys. Rev. E* **2016**, *93*, 033001.
[26] F. Cellini, F. Lavini, T. Cao, W. de Heer, C. Berger, A. Bongiorno, E. Riedo, *FlatChem* **2018**, *10*, 8.
[27] Y. Gao, T. Cao, F. Cellini, C. Berger, W. A. de Heer, E. Tosatti, E. Riedo, A. Bongiorno, *Nat. Nanotechnol.* **2018**, *13*, 133.
[28] K. V. Emtsev, A. Bostwick, K. Horn, J. Jobst, G. L. Kellogg, L. Ley, J. L. McChesney, T. Ohta, S. A. Reshanov, J. Röhrl, E. Rotenberg, A. K. Schmid, D. Waldmann, H. B. Weber, T. Seyller, *Nat. Mater.* **2009**, *8*, 203.
[29] Atomistica Software Suite, https://github.com/Atomistica/atomistica (accessed: April 2022).
[30] A. Hjorth Larsen, J. Jørgen Mortensen, J. Blomqvist, I. E. Castelli, R. Christensen, M. Dulak, J. Friis, M. N. Groves, B. Hammer, C. Hargus, E. D. Hermes, P. C. Jennings, P. Bjerre Jensen, J. Kermode, J. R. Kitchin, E. Leonhard Kolsbjerg, J. Kubal, K. Kaasbjerg, S. Lysgaard, J. Bergmann Maronsson, T. Maxson, T. Olsen, L. Pastewka, A. Peterson, C. Rostgaard, J. Schiøtz, O. Schütt, M. Strange, K. S. Thygesen, T. Vegge, et al., *J. Phys. Condens. Matter* **2017**, *29*, 273002.
[31] P. Grigorev, L. Frérot, F. Birks, A. Gola, J. Golebiowski, J. Grießer, J. L. Hörmann, A. Klemenz, G. Moras, W. G. Nöhring, J. A. Oldenstaedt, P. Patel, T. Reichenbach, T. Rocke, L. Shenoy, M. Walter, S. Wengert, L. Zhang, J. R. Kermode, L. Pastewka, *J. Open Source Softw.* **2024**, *9*, 5668.
[32] T. Reichenbach, L. Mayrhofer, T. Kuwahara, M. Moseler, G. Moras, *ACS Appl. Mater. Interfaces* **2020**, *12*, 8805.
[33] L. C. Ciacchi, D. J. Cole, M. C. Payne, P. Gumbsch, *J. Phys. Chem. C* **2008**, *112*, 12077.
[34] L. Pastewka, S. Moser, M. Moseler, *Tribol. Lett.* **2010**, *39*, 49.
[35] D. Frenkel, B. Smit, *Understanding Molecular Simulation*, Academic Press, New York **2002**.
[36] A. Stukowski, *Model. Simul. Mater. Sci. Eng.* **2010**, *18*, 015012.